AGU PUBLICATIONS

JGR

Journal of Geophysical Research: Space Physics

RESEARCH ARTICLE

10.1002/2014JA019779

Key Points:
- Solar wind velocity is the primary driver of electron variations at GEO
- Number and energy density and temperature are subject to v_{sw}-dependent lower limits
- A coarse predictive capability is obtained using solely this input parameter

Correspondence to:
D. P. Hartley,
d.hartley1@lancaster.ac.uk

Citation:
Hartley, D. P., M. H. Denton, and J. V. Rodriguez (2014), Electron number density, temperature, and energy density at GEO and links to the solar wind: A simple predictive capability, *J. Geophys. Res. Space Physics*, *119*, 4556–4571, doi:10.1002/2014JA019779.

Received 10 JAN 2014
Accepted 27 MAY 2014
Accepted article online 29 MAY 2014
Published online 18 JUN 2014

Electron number density, temperature, and energy density at GEO and links to the solar wind: A simple predictive capability

D. P. Hartley[1], M. H. Denton[1,2], and J. V. Rodriguez[3,4]

[1]Physics Department, University of Lancaster, Lancaster, UK, [2]Space Science Institute, Boulder, Colorado, USA, [3]National Oceanic and Atmospheric Administration, Boulder, Colorado, USA, [4]Cooperative Institute for Research in Environmental Sciences, University of Colorado Boulder, Boulder, Colorado, USA

Abstract Many authors have studied the outer radiation belts response to different solar wind drivers, with the majority investigating electron flux variations. Using partial moments (electron number density, temperature, and energy density) from GOES-13 during 2011 allows for changes in the number of electrons and the temperature of the electrons to be distinguished, which is not possible with the outputs of individual instrument channels. This study aims to produce a coarse predictive capability of the partial moments from GOES-13 by determining which solar wind conditions exhibit the strongest relationship with electron variations at GEO. Investigating how the electron distribution at GEO is affected by fluctuations in this primary driver, both instantaneous and time delayed, allows for this to be achieved. These predictive functions are then tested against data from 2012. It is found that using solely the solar wind velocity as a driver results in predicted values that accurately follow the general trend of the observed moments. This study is intended to make further progress in quantifying the relationship between the solar wind and electron number density, temperature, and energy density at GEO. Our results provide a coarse predictive capability of these quantities that can be expanded upon in future studies to incorporate other solar wind drivers to improve accuracy.

1. Introduction

Energetic electron fluxes at geosynchronous orbit (GEO) can be highly variable depending upon the state of the solar wind and its time history. Both coronal mass ejections and corotating interaction regions are known, upon impact with the magnetosphere, to cause variability in electron populations at GEO [*Borovsky and Denton*, 2006] from rapid decreases (*dropouts*) which can occur over a period of minutes [e.g., *Onsager et al.*, 2002; *Green et al.*, 2004; *Clilverd et al.*, 2013; *Hartley et al.*, 2013], to subsequent increases (*recoveries*) some hours or days later [*Freeman*, 1964; *Nagai*, 1988; *Chen et al.*, 2007; *Liemohn and Chan*, 2007; *Borovsky and Denton*, 2009]. The relationship between solar wind velocity and electron flux at GEO has long been established [*Paulikas and Blake*, 1979] and more recently revisited by *Reeves et al.* [2011]. Comparison of electron fluxes with various solar wind parameters (velocity, temperature, pressure, density, interplanetary magnetic field, etc.) has been the basis of many studies, with the primary aim being to obtain a predictive capability of radiation belt electrons for a given set of solar wind input parameters [e.g., *Nagai*, 1988; *Boynton et al.*, 2013; *Horne et al.*, 2013]. However, the complexity of the relationship between the solar wind and energetic electrons in the magnetosphere means that a reliable, accurate predictive model remains elusive. There have been many studies investigating the variability of radiation belt electrons and their response to different solar wind drivers [e.g., *Baker et al.*, 1986; *Hudson et al.*, 1997; *O'Brien et al.*, 2001; *Friedel et al.*, 2002; *Reeves et al.*, 2003; *Weigel et al.*, 2003; *Mann et al.*, 2004; *Li et al.*, 2005; *Borovsky and Denton*, 2006; *Liemohn and Chan*, 2007; *Millan and Thorne*, 2007; *Onsager et al.*, 2007; *Hudson et al.*, 2008, *Miyoshi and Kataoka*, 2008; *Borovsky and Denton*, 2010; *Morley et al.*, 2010; *Hartley et al.*, 2013, and references therein]. In addition, there is strong evidence that relativistic electrons are somewhat seasonally dependent [*Baker et al.*, 1999; *McPherron et al.*, 2009].

Recently *Reeves et al.* [2011, 2013] compared electron fluxes to solar wind drivers (primarily solar wind velocity) concluding that the electron flux distribution could not be explained by scatter about a linear relationship as previously considered, but rather a "triangle shape" distribution was revealed, with a velocity-dependent lower limit and a velocity-independent upper limit.

An alternative picture to that obtained by looking solely at the electron flux is provided by considering the electron temperature and number density at GEO [*Cayton et al.*, 1989; *Borovsky et al.*, 1998; *Denton et al.*, 2010; *Borovsky and Cayton*, 2011; *Denton and Cayton*, 2011]. A density and temperature description of the electron radiation belt has advantages over the traditional flux description. Changes in the number of electrons and changes in the temperature of the electrons are distinguishable. This is crucial since small variations in the temperature of the electron distribution may appear as order-of-magnitude changes in the relativistic-electron fluxes. Examination of the density and temperature reveals how the entire population respond to different conditions rather than the flux at a particular energy, thus providing an alternative picture of the evolution of the electron radiation belt, with the potential to reveal physical processes that may not be apparent with the traditional flux description (i.e., the measured flux at a particular energy is determined by changes in either the density or the temperature of the overall population). However, even with the density-temperature description used in this study, these are partial moments and therefore not sensitive to the entire population. It still remains unclear exactly how electrons in the outer radiation belt at GEO respond to solar wind velocity and density variations. By comparing partial moments (electron temperature and number density from GOES-13) with instantaneous and time-delayed solar wind conditions from the OMNI 2 database [*King and Papitashvili*, 2005], it is possible to investigate the complexity of the relationship and make further progress toward understanding the effect of solar wind conditions on electron temperature and number density at GEO.

In this study we summarize the primary solar wind drivers of electron number density and temperature at GEO as measured by GOES-13 during 2011. It appears that the 1 min resolution electron temperature and electron number density variations at GEO display some dependency on the solar wind proton density; however, the relationship with solar wind velocity is more well defined. Additionally, we find that both electron number density and temperature at GEO exhibit solar wind velocity-dependent lower limits (elevated temperature and number density at GEO only occur during, or some time after, fast solar wind). The electron energy density is also considered and is also found to be subject to a solar wind velocity-dependent lower limit. By producing fits to the data, we calculate a linear function that describes these upper/lower limits within given confidence bounds. This is done using instantaneous solar wind data, as well as time-delayed solar wind parameters in intervals of 12 h. Using time-delayed solar wind data and the calculated linear functions allows for a predictive capability of the electron number density, temperature, and energy density at GEO. These predictions are then tested against GOES-13 partial moments data from 2012 in order to study the accuracy of the calculated functions.

2. Instrumentation

The Magnetospheric Electron Detector (MAGED) onboard GOES-13 provides pitch angle-resolved flux measurements in the 30–600 keV energy range. Consisting of nine telescopes, each with a central pitch angle, α, defined by the orientation of the magnetic field measured by the GOES-13 magnetometer at any time, MAGED measures flux in five energy channels parameterized as 30–50, 50–100, 100–200, 200–350, and 350–600 keV. The fluxes are dead time and proton contamination corrected. The current NOAA real-time processing assumes a flat spectrum over each channel and mean central energies of 40, 75, 150, 275, and 475 keV. Using these electron measurements, it is possible to calculate the number density, n, and temperature, T, through the partial moments, equations (1)–(4), in addition to the energy density, $\mathcal{E}$, using equation (5).

$$n = 2\pi \iint f_v(\alpha, v)\, v^2 \sin(\alpha)\, \mathrm{d}\alpha\, \mathrm{d}v \tag{1}$$

$$T_{\mathrm{perp}} = \frac{\pi m}{n} \iint f_v(\alpha, v)\, v^4 \sin^3(\alpha)\, \mathrm{d}\alpha\, \mathrm{d}v \tag{2}$$

$$T_{\mathrm{para}} = \frac{2\pi m}{n} \iint f_v(\alpha, v)\, v^4 \cos^2(\alpha) \sin(\alpha)\, \mathrm{d}\alpha\, \mathrm{d}v \tag{3}$$

$$T = \frac{2T_{\mathrm{perp}} + T_{\mathrm{para}}}{3} \tag{4}$$

$$\mathcal{E} = nT \tag{5}$$

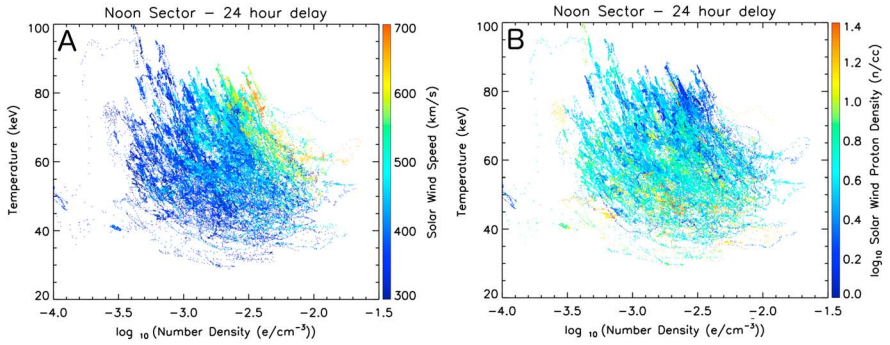

Figure 1. Variability of partial moments (electron number density and temperature) measured at GEO by GOES-13 with (a) solar wind velocity and (b) density for a 24 h time delay in the noon sector.

where $f_v(\alpha, v)$ is a velocity distribution converted from differential flux as a function of the central pitch angle of each telescope.

The calculation of partial moments, although based on a Maxwellian formulation, does not use a Maxwellian fit, unlike the work of *Cayton et al.* [1989]. Rather, it approximates the integrals as weighted two-dimensional sums of the velocity distribution at each measured energy and pitch angle. The velocity distribution is approximated as uniform across the energy range of each channel listed above and between pitch angle limits defined as the average of the telescope central pitch angles, with the lowest limit set to 0° and the highest limit set to 90°. Due to the sparse pitch angle sampling, fluxes with pitch angles between 90 and 180° are assigned to the supplement of their pitch angle, and the sum from 0 to 90° is doubled in calculating the integral. For the electrons, relativistic versions of equations (1)–(3) are used, but the difference at MAGED energies is only a few percent. The electron energy density, $\mathcal{E}$, is also considered [*Gurgiolo et al.*, 1979; *Daglis et al.*, 1994]. This is calculated by removing the number density denominator in the temperature integrals (multiplying the partial number density by partial temperature). This is investigated in order to consider any artificial anticorrelation between the electron number density and temperature caused by the partial nature of the GOES-13 moments. Since theory suggests that these parameters may be anticorrelated in general [*Scudder*, 1992], it is crucial to be aware of this possible artificial behavior.

Cayton et al. [1989] found that the electron energy distribution at geosynchronous orbit could be well described by Maxwellian distributions. (It is also noted that *Pierrard and Lemaire* [1996] found that the electron energy spectra away from geosynchronous orbit could also be well described by Maxwellians). While the Maxwellian distribution is not to be the only possible representation of radiation belt electrons (the kappa distribution is also commonly used), it has shown to be a useful representation [e.g., *Gary*, 1993; *Onsager et al.*, 2004; *MacDonald et al.*, 2008; *Denton et al.*, 2010; *Denton and Cayton*, 2011; *Clilverd et al.*, 2013]. Since the Maxwellian distribution is a limiting case of the kappa distribution [e.g., *Christon et al.*, 1988; *Gkioulidou et al.*, 2009], it is important to establish the behavior of the simpler model before investigating the more general model. It should also be noted that the quantities of energy density and number density are model independent.

3. Analysis and Results

The methodology used in this study is designed to

1. Determine which solar wind parameter displays the strongest relationship with the electron number density, temperature, and energy density at GEO (both instantaneous and time delayed in 12 h intervals).
2. Investigate how the distributions of electron number density, temperature, and energy density at GEO vary with this driving solar wind parameter (both instantaneous and time delayed in 12 h intervals).
3. Calculate linear fits to these distributions (instantaneous and time delayed) in order to obtain, given a measurement of the primary solar wind driver, a prediction of the electron number density, temperature, and energy density at GEO in intervals of 12 h in the future.
4. Test how accurate these calculated functions are at predicting the electron number density, temperature, and energy density at GEO.

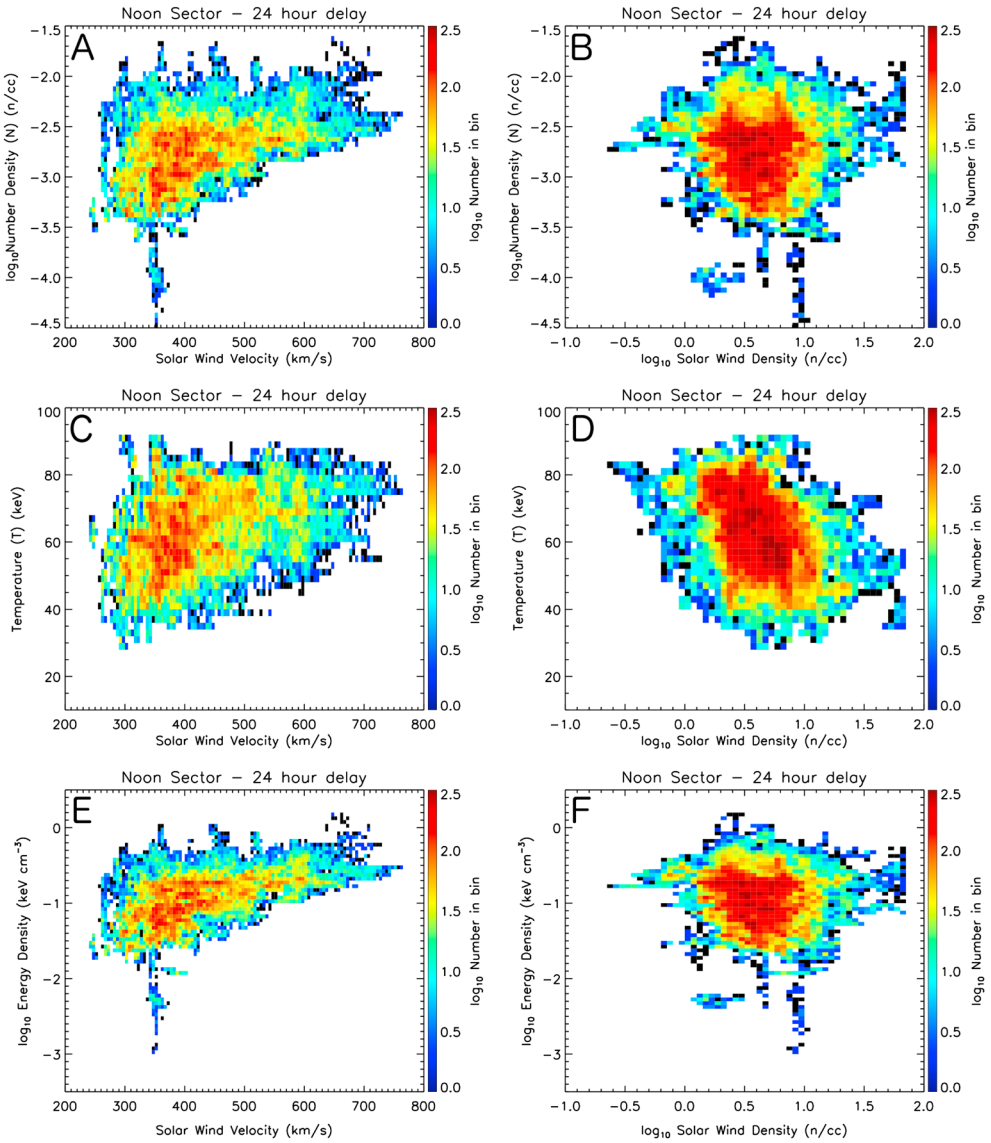

Figure 2. Density plots displaying the partial moments (electron number density, temperature, and energy density) from GOES-13 at GEO for varying solar wind conditions with a time delay of 24 h applied; (a, c, e) solar wind velocity and (b, d, f) solar wind density.

3.1. Determining the Primary Driver

One minute resolution electron temperature and number density from GOES-13 at GEO during 2011 are calculated using equations (1)–(4). Additionally, the electron energy density is calculated by multiplying the electron temperature by the number density (see equation (5)). Initially, we compare these partial moments with solar wind velocity and density in order to establish the primary driving solar wind parameter. This is done by comparing the partial moments from GOES-13 with solar wind measurements in intervals of 12 h prior, from 48 h to instantaneous. We also consider a negative 12 h delay (partial moments from GOES-13 observed 12 h prior to the solar wind measurements). While no causal relationship can exist between the GOES observations and the solar wind parameters observed 12 h in the future, this is included in order to provide a baseline from which to compare any apparent structure that may exist with increasing time delays.

Figure 1a displays each 1 min resolution electron temperature and number density measurement at GEO by GOES-13 during 2011 for all local time sectors, with the color indicating the solar wind velocity for one time delay, 24 h (warm colors indicate elevated velocities, cool colors indicate slower velocities). Figure 1b displays the same parameters with the color this time indicating the solar wind density (warm colors indicate

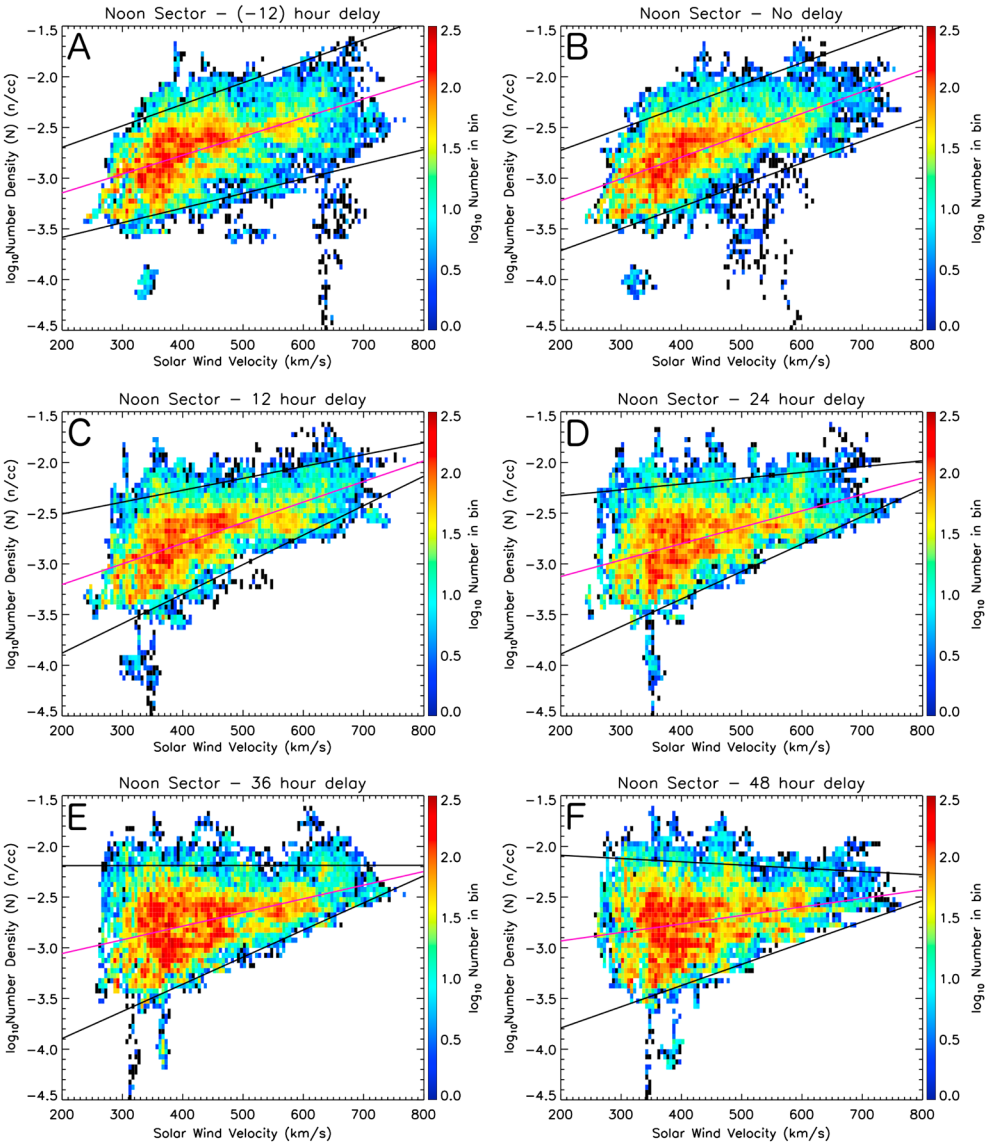

Figure 3. Density plots of solar wind velocity against electron number density at GEO in the noon sector for increasing time delay. (a) Negative 12 h delay, (b) instantaneous, (c) 12 h delay, (d) 24 h delay, (e) 36 h delay, and (f) 48 h delay. The pink line indicates the median number density for each solar wind velocity bin, while the straight black lines indicate a linear fit of the mean ± 2 standard deviations for each solar wind velocity bin (lower and upper bounds). Equations describing these upper and lower bounds, as well as the predicted quantity, are listed on the equation (6) with coefficients listed in Table 1.

elevated densities, cool colors indicate lower densities). These figures exhibit similarities to that displayed by *Denton et al.* [2010] for the "soft component" of the relativistic Maxwellian fits to Los Alamos National Laboratory (LANL)-01a spacecraft data for the years 2001–2007. The temperatures calculated for GOES-13 are significantly higher than those from LANL-01a, since the soft component has an upper limit of 300 keV and MAGED has an additional channel (350–600 keV) above that limit. This analysis was performed for a range of time delays (−12 h, 0 h, 12 h, 24 h, 36 h, and 48 h), with no large increase or decrease in structure apparent. To calculate the time delay, we simply take the solar wind velocity measurement from the number of delay hours prior to the GOES observation (i.e., GOES[n] corresponds to OMNI[$n - (i \times 60)$] for i hour delay and data at 1 min time intervals).

For the solar wind velocity (Figure 1a), it is apparent that elevated number density and elevated temperature occur independently 24 h following a broad range of solar wind velocities. However, for both to be simultaneously elevated, the solar wind speed must have been elevated [*Borovsky and Denton*, 2010; *Denton et al.*,

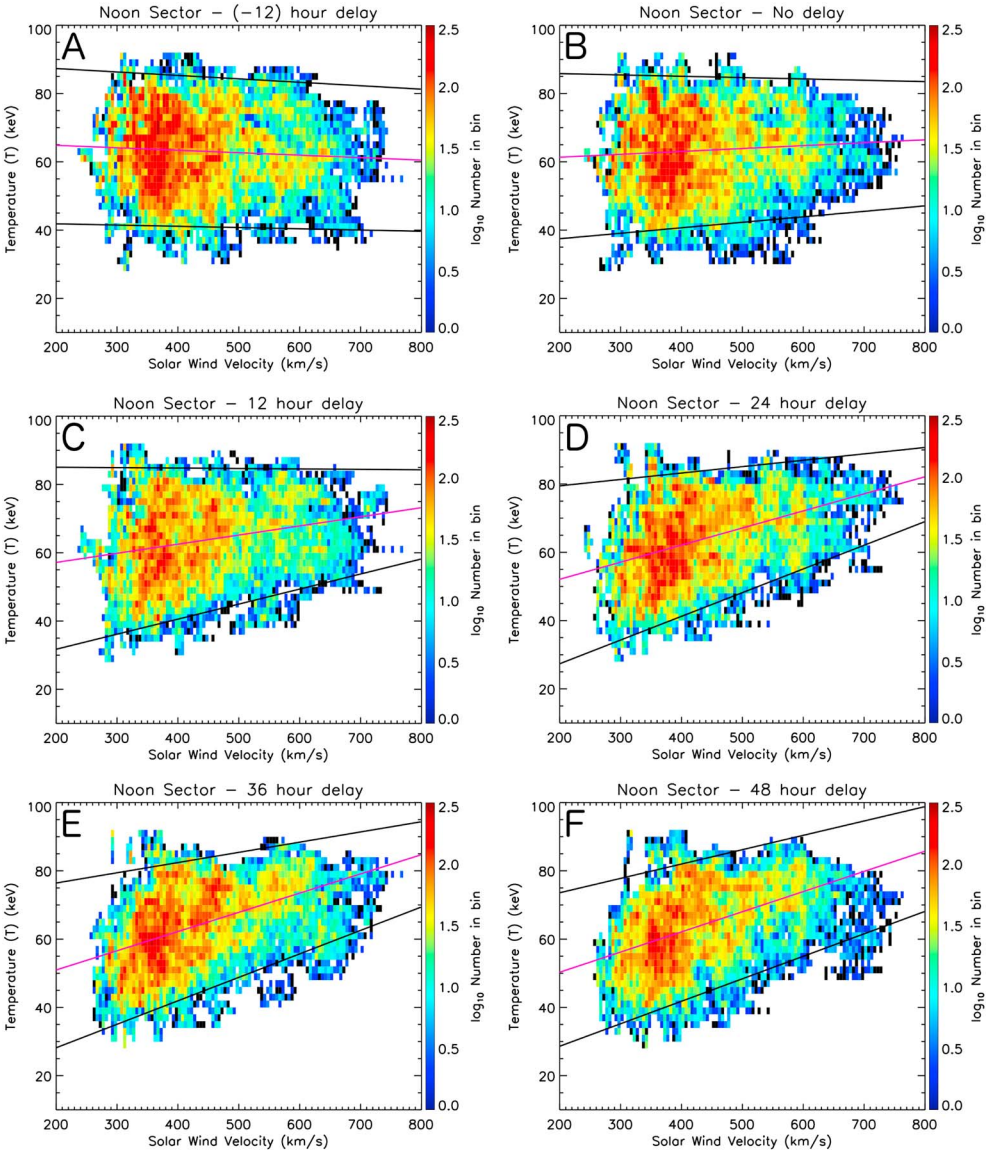

Figure 4. Density plots of solar wind velocity against electron temperature at GEO in the noon sector for increasing time delay. (a) Negative 12 h delay, (b) instantaneous, (c) 12 h delay, (d) 24 h delay, (e) 36 h delay, and (f) 48 h delay. The pink line indicates the median temperature for each solar wind velocity bin, while the straight black lines indicate a linear fit of the mean ± 2 standard deviations for each solar wind velocity bin (lower and upper bounds). Equations describing these upper and lower bounds, as well as the predicted quantity, are listed on the equation (7) with coefficients listed in Table 2.

2010; *Borovsky and Cayton*, 2011; *Denton and Cayton*, 2011]. It is noted that there are clear inverse law striations apparent in Figure 1 which may be, at least partly, attributable to the number density denominator in the temperature integrals. To remove this behavior, the electron energy density is also considered during this study.

When comparing the electron number density and temperature to the solar wind density (Figure 1b) there is also some structure apparent. Elevated electron temperature and number density at GEO primarily occur during periods of depleted solar wind density (note that elevated electron fluxes have also been shown to occur at low solar wind densities by *Balikhin et al.* [2011]). However, it appears that there is a more well-defined structure when considering the solar wind velocity instead of the solar wind density.

In order to further investigate this relationship, data are binned based upon the solar wind conditions 24 h prior in 5 km s^{-1} solar wind velocity bins and 0.05 $\log_{10}$ cm^{-3} solar wind density bins. Additional binning is

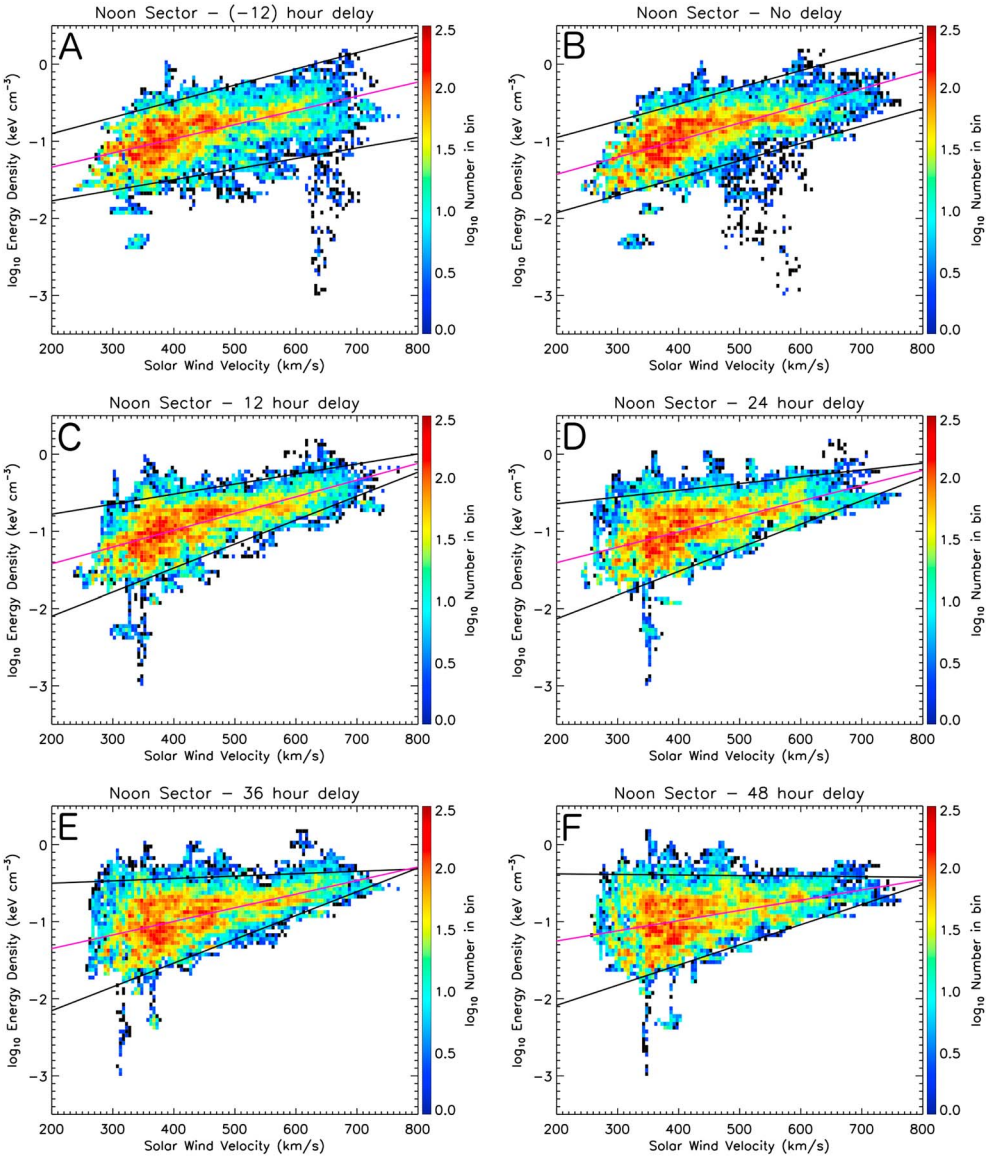

Figure 5. Density plots of solar wind velocity against electron energy density at GEO in the noon sector for increasing time delay. (a) Negative 12 h delay, (b) instantaneous, (c) 12 h delay, (d) 24 h delay, (e) 36 h delay, and (f) 48 h delay. The pink line indicates the median energy density for each solar wind velocity bin, while the straight black lines indicate a linear fit of the mean ± 2 standard deviations for each solar wind velocity bin (lower and upper bounds). Equations describing these upper and lower bounds, as well as the predicted quantity, are listed on the equation (8) with coefficients listed in Table 3.

performed for the electron number density, temperature, and energy density from GOES-13. The logarithm of the number density is binned in intervals of 0.05 $\log_{10}$ cm^{-3}, the temperature is binned in intervals of 2 keV, and the logarithm of the electron energy density is binned in intervals of 0.05 $\log_{10}$ keV cm^{-3}. We then display the number of occurrences recorded in each bin in color. These results are shown in Figure 2.

For the solar wind velocity, Figures 2a, 2c, and 2e, it is apparent that as velocity increases, the minimum observed electron temperature, number density, and energy density also increase (velocity-dependent lower limit). This is not the case when comparing the partial moments with the solar wind density (Figures 2b, 2d, and 2f) which does not display a clear structure.

Our results suggest that the electron temperature, electron number density, and electron energy density variations at GEO display some dependency on the solar wind density; however, the relationship with solar wind velocity is more well defined.

Table 1. A Table Showing the Parameters to be Used in Equation (6) to Calculate the Predicted Value, the Lower Bound, and the Upper Bound of the Electron Number Density at GEO for Five Different Time Delays (0 h, 12 h, 24 h, 36 h, and 48 h) for Four Local Time Sectors at GEO

	Number Density (cm^{-3})					
	Prediction		Lower Bound		Upper Bound	
Delay	$c_0(N)$	$c_1(N)$	$c_0(N)$	$c_1(N)$	$c_0(N)$	$c_1(N)$
			Noon Sector			
0 h	2.15×10^{-3}	−3.65	2.16×10^{-3}	−4.15	2.16×10^{-3}	−3.16
12 h	2.03×10^{-3}	−3.61	2.91×10^{-3}	−4.46	1.17×10^{-3}	−2.74
24 h	1.62×10^{-3}	−3.45	2.72×10^{-3}	−4.43	0.57×10^{-3}	−2.44
36 h	1.35×10^{-3}	−3.33	2.67×10^{-3}	−4.43	0.00×10^{-3}	−2.19
48 h	0.84×10^{-3}	−3.10	2.09×10^{-3}	−4.21	-0.32×10^{-3}	−2.02
			Midnight Sector			
0 h	1.96×10^{-3}	−3.66	0.39×10^{-3}	−3.80	3.52×10^{-3}	−3.59
12 h	2.16×10^{-3}	−3.77	2.17×10^{-3}	−4.53	2.35×10^{-3}	−3.11
24 h	1.87×10^{-3}	−3.66	2.40×10^{-3}	−4.64	1.60×10^{-3}	−2.78
36 h	1.39×10^{-3}	−3.46	2.14×10^{-3}	−4.57	0.94×10^{-3}	−2.47
48 h	1.17×10^{-3}	−3.36	2.17×10^{-3}	−4.60	0.43×10^{-3}	−2.24
			Dusk Sector			
0 h	1.84×10^{-3}	−3.62	0.97×10^{-3}	−3.857	2.32×10^{-3}	−3.28
12 h	1.89×10^{-3}	−3.65	3.03×10^{-3}	−4.67	0.86×10^{-3}	−2.71
24 h	1.76×10^{-3}	−3.60	3.14×10^{-3}	−4.74	0.44×10^{-3}	−2.51
36 h	1.34×10^{-3}	−3.42	2.83×10^{-3}	−4.62	0.08×10^{-3}	−2.35
48 h	1.13×10^{-3}	−3.34	2.81×10^{-3}	−4.64	-0.32×10^{-3}	−2.16
			Dawn Sector			
0 h	2.50×10^{-3}	−3.78	1.83×10^{-3}	−4.10	3.35×10^{-3}	−3.46
12 h	2.30×10^{-3}	−3.71	2.29×10^{-3}	−4.34	2.49×10^{-3}	−3.07
24 h	1.80×10^{-3}	−3.50	2.32×10^{-3}	−4.38	1.69×10^{-3}	−2.69
36 h	1.50×10^{-3}	−3.38	2.50×10^{-3}	−4.49	0.82×10^{-3}	−2.30
48 h	1.11×10^{-3}	−3.21	2.22×10^{-3}	−4.39	0.13×10^{-3}	−1.99

3.2. Distribution of Partial Moments With Varying Primary Solar Wind Driver

Having established that the solar wind velocity has a stronger relationship with the electron number density, temperature, and energy density variations at GEO than the solar wind density, we investigate the variations of the GOES-13 moments with solar wind velocity in more detail. Due to inherent local time variations, we sort GOES-13 measurements in local time, binning data into four local time bins (Dawn 4–8 LT, Noon 10–14 LT, Dusk 16–20 LT, and Midnight 22–2 LT). From this point forward we display results from the noon sector only, although the analysis is repeated for all local time sectors. Studying the number of occurrences of electron number density, temperature, and energy density in small solar wind velocity intervals allows for the distribution of GOES-13 partial moments with respect to the solar wind velocity to be obtained. Figures 3–5 display the results of this analysis. Data are binned in 5 km s^{-1} solar wind velocity bins. Additional binning is performed for the electron number density, temperature, and energy density from GOES-13. The logarithm of the number density is binned in intervals of 0.05 $\log_{10}$ cm^{-3}, the temperature is binned in intervals of 2 keV, and the logarithm of the energy density is binned in intervals of 0.05 $\log_{10}$ keV cm^{-3}. We then display the number of occurrences recorded in each bin in color. Displaying data in this way allows for more detail of the distributions to be shown than merely producing a scatterplot. Figure 3 displays the distributions of electron number density at GEO for time delays from (−12) h to 48 h in intervals of 12 h. Figures 4 and 5 contain the same analysis repeated for the electron temperature and energy density at GEO, respectively.

First, considering the electron number density (Figure 3), it is apparent that elevated number densities can occur simultaneous to, or several hours following, a broad range of solar wind velocities; however, there are few instances where a high solar wind velocity results in a low electron number density at GEO. This result, when observed using electron fluxes, lead to the suggestion of a velocity-dependent lower limit on the electron flux [*Reeves et al.*, 2011, 2013]. The results in Figure 3 (for positive delays) show that this also appears to be the case with the electron number density as measured by GOES-13. It is noteworthy that

Table 2. A Table Showing the Parameters to be Used in Equation (7) to Calculate the Predicted Value, the Lower Bound, and the Upper Bound of the Electron Temperature at GEO for Five Different Time Delays (0 h, 12 h, 24 h, 36 h, and 48 h) for Four Local Time Sectors at GEO

	Temperature (keV)					
	Prediction		Lower Bound		Upper Bound	
Delay	$c_0(T)$	$c_1(T)$	$c_0(T)$	$c_1(T)$	$c_0(T)$	$c_1(T)$
			Noon Sector			
0 h	0.85×10^{-2}	59.6	1.61×10^{-2}	34.3	-0.39×10^{-2}	86.6
12 h	2.67×10^{-2}	51.8	4.41×10^{-2}	22.9	-0.13×10^{-2}	85.3
24 h	5.00×10^{-2}	42.1	6.94×10^{-2}	13.5	1.87×10^{-2}	75.7
36 h	5.63×10^{-2}	39.7	6.87×10^{-2}	14.5	2.99×10^{-2}	70.5
48 h	5.91×10^{-2}	38.5	6.58×10^{-2}	15.5	4.21×10^{-2}	65.2
			Midnight Sector			
0 h	-0.87×10^{-2}	60.7	-1.98×10^{-2}	41.3	-0.16×10^{-2}	80.5
12 h	2.33×10^{-2}	47.4	0.66×10^{-2}	30.3	2.48×10^{-2}	69.4
24 h	3.81×10^{-2}	41.3	2.35×10^{-2}	24.3	3.49×10^{-2}	64.2
36 h	5.02×10^{-2}	36.5	3.40×10^{-2}	20.1	5.24×10^{-2}	56.7
48 h	5.35×10^{-2}	35.1	3.65×10^{-2}	19.3	5.19×10^{-2}	56.9
			Dusk Sector			
0 h	2.09×10^{-2}	53.3	1.34×10^{-2}	35.4	2.16×10^{-2}	73.7
12 h	4.23×10^{-2}	44.3	6.03×10^{-2}	17.5	1.81×10^{-2}	73.9
24 h	5.86×10^{-2}	37.2	7.16×10^{-2}	13.2	3.34×10^{-2}	66.6
36 h	6.28×10^{-2}	35.8	7.59×10^{-2}	12.2	4.05×10^{-2}	63.4
48 h	6.09×10^{-2}	36.6	7.46×10^{-2}	12.9	4.53×10^{-2}	60.8
			Dawn Sector			
0 h	-2.40×10^{-2}	67.2	-2.22×10^{-2}	43.3	-1.86×10^{-2}	88.1
12 h	1.01×10^{-2}	53.1	0.25×10^{-2}	32.7	0.55×10^{-2}	78.2
24 h	3.03×10^{-2}	45.2	1.67×10^{-2}	27.1	2.32×10^{-2}	70.5
36 h	3.76×10^{-2}	42.1	2.10×10^{-2}	25.4	3.48×10^{-2}	64.9
48 h	4.45×10^{-2}	39.3	2.20×10^{-2}	25.4	4.74×10^{-2}	59.5

there is little quantifiable difference between the negative 12 h delay plot (Figure 3a) and the plot for zero delay (Figure 3b), thus indicating that the consideration of a time delay is imperative.

Second, we study the electron temperature at GEO (Figure 4). With no time delay, the electron temperature appears to have little relationship to solar wind velocity, with both elevated and low temperatures occurring across a broad range of solar wind velocities. However, as the time delay is increased, a velocity-dependent lower limit of the electron temperature becomes increasingly apparent (24 h delay, 36 h delay, and 48 h delay). Therefore, elevated temperatures only occur some time after the arrival of fast solar wind. This is consistent with the results of *Borovsky and Denton* [2010] who showed that the temperature of the electron distribution at GEO increases during the fast solar wind following the passing of a corotating interaction region. Again, it is noted that there is little difference between negative 12 h delay and zero delay (Figures 4a and 4b).

Third, we study the energy density of electrons at GEO (Figure 5). The energy density exhibits similar structure to the electron number density with elevated energy densities occurring over a broad range of solar wind velocities and few instances where an elevated solar wind velocity results in a low-energy density of electrons at GEO (velocity-dependent lower limit). Considering the energy density, thus removing the number density denominator dependence on the electron temperature, appears to increase the correlation of the second moment with solar wind velocity. This should therefore increase chances of obtaining a more accurate predictive capability for this moment.

3.3. Calculating Prediction Functions

Using the distributions presented in Figures 3–5, linear functions are calculated in order to quantify the observed velocity-dependent lower limit, upper limit, and average of the observed quantity for instantaneous and positive time delays only. Other databased modeling techniques are noted (e.g., ARMAX [*Johansson*, 1993; *Ljung*, 1999; *Nelles*, 2001], neural networks [*Koons and Gorney*, 1991; *Fukata et al.*, 2002], and NARMAX [*Balikhin et al.*, 2011; *Boynton et al.*, 2013]); however, a simple single-term linear method was

Table 3. A Table Showing the Parameters to be Used in Equation (8) to Calculate the Predicted Value, the Lower Bound, and the Upper Bound of the Electron Energy Density at GEO for Five Different Time Delays (0 h, 12 h, 24 h, 36 h, and 48 h) for Four Local Time Sectors at GEO

	Energy Density (keV cm^{-3})					
	Prediction		Lower Bound		Upper Bound	
Delay	$c_0(\mathcal{E})$	$c_1(\mathcal{E})$	$c_0(\mathcal{E})$	$c_1(\mathcal{E})$	$c_0(\mathcal{E})$	$c_1(\mathcal{E})$
			Noon Sector			
0 h	2.22×10^{-3}	−1.87	2.25×10^{-3}	−2.38	2.17×10^{-3}	−1.39
12 h	2.17×10^{-3}	−1.86	3.11×10^{-3}	−2.72	1.30×10^{-3}	−1.04
24 h	2.00×10^{-3}	−1.81	3.06×10^{-3}	−2.74	0.88×10^{-3}	−0.82
36 h	1.76×10^{-3}	−1.70	3.08×10^{-3}	−2.77	0.31×10^{-3}	−0.56
48 h	1.32×10^{-3}	−1.52	2.61×10^{-3}	−2.61	-0.07×10^{-3}	−0.37
			Midnight Sector			
0 h	2.01×10^{-3}	−1.91	0.33×10^{-3}	−2.06	3.39×10^{-3}	−1.77
12 h	2.36×10^{-3}	−2.08	2.35×10^{-3}	−2.87	2.41×10^{-3}	−1.38
24 h	2.15×10^{-3}	−2.00	2.71×10^{-3}	−3.03	1.74×10^{-3}	−1.10
36 h	1.87×10^{-3}	−1.90	2.54×10^{-3}	−2.99	1.21×10^{-3}	−0.84
48 h	1.63×10^{-3}	−1.79	2.68×10^{-3}	−3.07	0.59×10^{-3}	−0.57
			Dusk Sector			
0 h	2.09×10^{-3}	−1.93	0.94×10^{-3}	−2.09	2.60×10^{-3}	−1.58
12 h	2.19×10^{-3}	−1.98	3.38×10^{-3}	−3.05	1.09×10^{-3}	−1.00
24 h	2.17×10^{-3}	−1.98	3.58×10^{-3}	−3.15	0.76×10^{-3}	−0.85
36 h	1.78×10^{-3}	−1.81	3.33×10^{-3}	−3.05	0.42×10^{-3}	−0.70
48 h	1.62×10^{-3}	−1.76	3.47×10^{-3}	−3.14	-0.12×10^{-3}	−0.44
			Dawn Sector			
0 h	2.39×10^{-3}	−1.96	1.86×10^{-3}	−2.31	2.99×10^{-3}	−1.62
12 h	2.37×10^{-3}	−1.96	2.51×10^{-3}	−2.61	2.34×10^{-3}	−1.34
24 h	2.04×10^{-3}	−1.83	2.70×10^{-3}	−2.70	1.63×10^{-3}	−1.01
36 h	1.86×10^{-3}	−1.76	3.02×10^{-3}	−2.87	0.73×10^{-3}	−0.61
48 h	1.40×10^{-3}	−1.58	2.78×10^{-3}	−2.80	-0.10×10^{-3}	−0.31

selected in order to easily quantify the limits (upper/lower/median) of the observed "triangle shape" distributions and obtain a first-order predictive capability. This data-driven modeling technique is purely for GEO and may be useful for other models that require the conditions at GEO as boundary conditions. These linear functions are displayed in Figures 3–5; lower and upper limits in black and average observed quantity in pink. As these functions are calculated for several time delays, using them should allow for a prediction to be made in intervals of 12 h in the future following a solar wind observation. In order to quantify the velocity-dependent lower and upper limits, the mean $\pm 2\sigma$ (where σ is the standard deviation) is calculated for each solar wind velocity bin. A linear fit through these values is then produced (black). This encapsulates $\sim 90\%$ of the data and is therefore considered to be a 90% confidence bound on the data. Additionally, the median value in each solar wind velocity bin is calculated, with a linear fit through these values produced (pink). The result is a function whereby $\sim 50\%$ of the data lies above and $\sim 50\%$ below. This is the predicted value of the electron number density/temperature/energy density at GEO. These linear functions are displayed in Figures 3–5 (black lines indicating the 90% confidence bound and the pink line indicating the predicted quantity). The equations describing these functions are listed as equations (6)–(8) with coefficients ($c_0(N)$, $c_1(N)$, $c_0(T)$, $c_1(T)$, $c_0(\mathcal{E})$, and $c_1(\mathcal{E})$) listed in Tables 1–3 for all local time sectors. These calculated functions have a validity range of solar wind velocities between 250 km s^{-1} and 750 km s^{-1}.

$$N\left(\mathrm{cm}^{-3}\right) = 10^{c_0(N)V_{SW}+c_1(N)} \tag{6}$$

$$T\,(\mathrm{keV}) = c_0(T)V_{SW} + c_1(T) \tag{7}$$

$$\mathcal{E}\left(\mathrm{keV\,cm}^{-3}\right) = 10^{c_0(\mathcal{E})V_{SW}+c_1(\mathcal{E})} \tag{8}$$

For zero delay, the electron number density distribution in the noon sector (Figure 3b) can be explained by scatter about a linear trend, since the gradient of the upper and lower bound, as well as the predicted value,

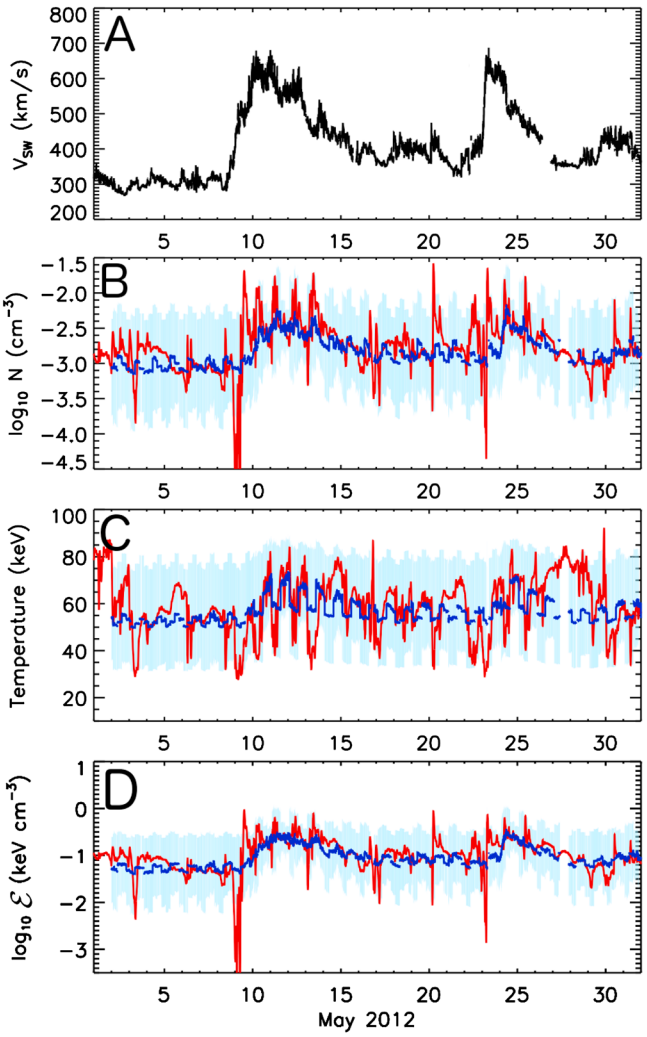

Figure 6. (a) The solar wind velocity during May 2012; (b) the electron number density at geosynchronous orbit measured by GOES-13 (red), the prediction as calculated 24 h in advance (dark blue), and the upper and lower bounds to 90% confidence limits (blue shading); (c) the electron temperature at geosynchronous orbit measured by GOES-13 (red), the prediction as calculated 24 h in advance (dark blue), and the upper and lower bounds to ~90% confidence limits (blue shading); and (d) the electron energy density at geosynchronous orbit measured by GOES-13 (red), the prediction as calculated 24 h in advance (dark blue), and the upper and lower bounds to ~ 90% confidence limits (blue shading).

are approximately equal. However, with the addition of a time delay (Figures 3c–3f), a velocity-dependent lower limit becomes increasingly apparent. This leads to the conclusion that for any given time, knowing the instantaneous solar wind velocity allows for a prediction of the minimum electron number density at GEO at some time in the future. With regards to a velocity-dependent upper limit, as larger time delays are applied the calculated gradient of this limit decreases. This indicates that the upper limit is not dependent upon the solar wind velocity.

With no time delay, the electron temperature (Figure 4b) appears to have little relationship to solar wind velocity, with both elevated and decreased temperatures occurring across a broad range of solar wind velocities. The median line (pink) is relatively flat, varying very little with solar wind velocity. As the time delay is increased (Figures 4c–4f), a velocity-dependent lower limit of the electron temperature becomes increasingly apparent (24 h delay, 36 h delay, and 48 h delay). Thus, elevated temperatures only occur some time after fast solar wind. The gradient of the velocity-dependent lower bound is steepest when a time delay of 24 h is applied although remains relatively well defined up to 48 h delay.

The energy density of electrons at GEO appears similar in structure to the electron number density. With zero delay, the energy density distribution in the noon sector (Figure 5b) could be explained by scatter about a linear trend, since there is little difference between the gradient of the upper bound, lower bound, and the predicted quantity. However, as with the electron number density, with the addition of a time delay, the distribution becomes more like the "triangle distributions" observed for electron fluxes by *Reeves et al.* [2011].

This method is then repeated for the dawn, dusk, and midnight local time sectors with calculated coefficients $c_0(N)$, $c_1(N)$, $c_0(T)$, $c_1(T)$, $c_0(\mathcal{E})$, and $c_1(\mathcal{E})$ listed in Tables 1–3. The calculated gradient coefficients for the predicted quantities are generally larger in the noon sector than in the midnight sector for all quantities, with the intercept coefficients also larger in the noon sector than in the midnight sector for the majority of time delays. This is consistent with the results of *Borovsky and Denton* [2010] who concluded that the outer electron radiation belt at local noon at GEO is hotter than the outer electron radiation belt at local midnight at GEO.

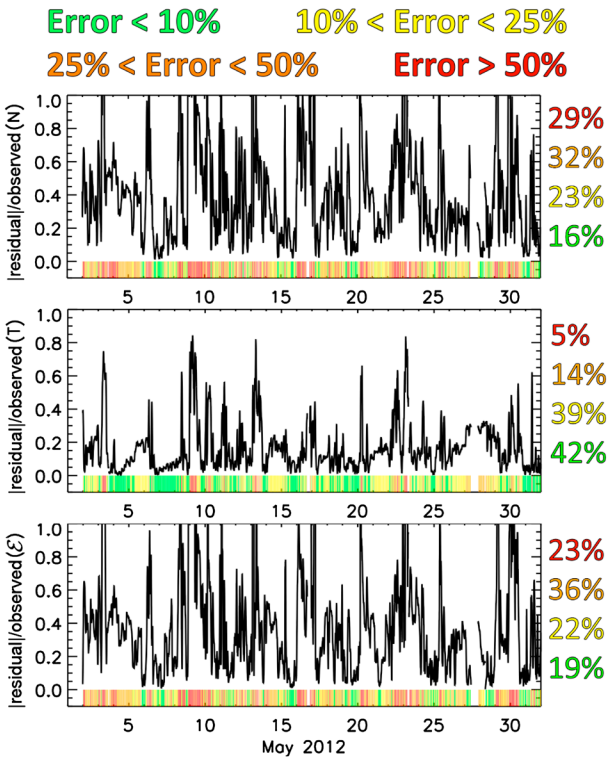

Figure 7. (top to bottom) Figure showing the percentage error (magnitude of the residual divided by the observed quantity) for the same time period and delay shown in Figure 6 (May 2012, 24 h delay). The figure also contains a color indicator at the bottom of each panel in order to show the magnitude of the percentage error; less than 10% (green), between 10% and 25% (yellow), between 25% and 50% (orange), and greater than 50% (red). Also, listed on the figure is the percentage of the time period whereby the percentage error falls in the bounds defined above.

3.4. Testing the Prediction

Having used data from GOES-13 throughout the duration of 2011 to calculate coefficients to a linear function that relates the solar wind velocity to the electron number density, temperature, and energy density at GEO in four local time sectors, we now test this relationship using GOES-13 moments data from 2012 and a time delay of 24 h. The 24 h lag was chosen since *Denton and Borovsky* [2009] showed that the time between observed solar wind velocity variations and associated variations in the plasma sheet density was between 8 and 18 h (depending on LT). Given that the plasma sheet is the seed population for the electron radiation belt, it followed to use a solar wind velocity delay greater than 18 h; hence, 24 h was selected. Figure 6 displays the solar wind velocity for May 2012, the electron number density, temperature, and energy density as measured by GOES-13 at GEO (red) during the same period, in addition to the predicted value (dark blue) and the 90% confidence bounds (pale blue shading) for electron number density, temperature, and energy density as calculated in this study. Having calculated these coefficients for 4 h local time sectors centered around dawn/noon/dusk/midnight, these coefficients are then applied to larger, 6 h local time sectors. Due to the method used in this study, the calculated coefficients change as the spacecraft crosses between local time sectors. This results in discontinuities or "stepping" (apparent in Figure 6) of the predicted values between local time sectors. While this behavior is not physical and merely an artifact of binning the data, it does capture the trends of the general local time variations.

For the electron number density (Figure 6b), the calculated values appear to quite closely follow the overarching trend throughout the month. There are some large discrepancies although these do occur during highly dynamic periods in the measured number density which are likely caused by electron dropouts at GEO or substorm injections. During the most extreme of these cases (i.e., on 9, 20, and 23 May), the measured quantity does fall outside of our shaded 90% confidence bounds; however, these do not occur frequently.

Considering the electron temperature (Figure 6c), the predicted values again follow the general trend of the measured temperature from GOES-13. There are again periods where large discrepancies do occur, primarily between 27 and 29 May. The discrepancy during this period is likely due to the passing of the two high-speed solar wind streams resulting in elevated fluxes in the 350–600 keV energy range, thus elevating the temperature considerably. It is also noted that during this period there are few substorm injections; hence, the temperature remains elevated and does not decrease around midnight. The measured temperature does occasionally fall outside of the shaded pale blue 90% confidence bounds, however, not frequently. Although given the large range encapsulated by the pale blue bounds, this result is not surprising.

For the energy density, (Figure 6d), the predicted values closely follow the general trend of the observed quantity. Outside of the large reductions in energy density observed on 9 and 23 May, the observed value

rarely falls outside of the calculated pale blue limits. The variability in energy density appears to be more easily predicted than the electron temperature when using the methodology implemented in this study. This is due to the higher correlation of electron energy density at GEO with solar wind velocity compared to electron temperature.

Figure 7 displays a quantitative analysis of the residuals between the predicted (median) and observed parameters for the same time period (May 2012) and delay (24 h) as in Figure 6. The percentage error (magnitude of the residual divided by the observed quantity) is shown for number density (top), temperature (middle), and energy density (bottom). At the bottom of each figure panel is a color indicator showing the magnitude of the percentage error at each time interval; less than 10% (green), between 10% and 25% (yellow), between 25% and 50% (orange), and greater than 50% (red). Also, listed next to each figure panel is the percentage of the time period whereby the percentage error falls in the defined bounds. That is, for number density (top), this method yields values that are accurate to within 50%, 71% of the time (sum of green yellow and orange), and accurate to within 25% (sum of green and yellow), 39% of the time. For temperature (middle), this method yields values that are accurate to within 50%, 95% of the time, and accurate to within 25%, 81% of the time. For energy density (bottom), this method yields values that are accurate to within 50%, 77% of the time, and accurate to within 25%, 41% of the time.

It is apparent that the solar wind velocity plays a large role in driving the electron number density, temperature, and energy density at GEO, with a coarse predictive capability acquired using solely this quantity as input. This study provides a simple method of predicting the electron number density, temperature, and energy density at GEO for different time scales in the future that has shown to produce results that follow the general trend of observations.

4. Discussion and Conclusions

This study provides insight into the driving of electron number density, temperature, and energy density in four local time sectors at GEO by the solar wind. Both solar wind velocity and density exhibit a relationship with the variation of the electron number density, temperature, and energy density calculated from GOES-13, with the relationship to solar wind velocity more well defined than that of the solar wind density. Elevated electron temperatures and number densities in the outer electron radiation belt can occur during slow solar wind, however, for both elevated electron temperature and elevated electron number density to occur simultaneously, elevated solar wind speed is required, either instantaneous or some time in the previous 48 h. Solar wind velocity-dependent lower limits are visible in electron temperature, number density, and energy density at GEO, similar to the triangle shape uncovered by *Reeves et al.* [2011] for electron flux, with the limits becoming clearer with the addition of a time delay. A function describing this velocity-dependent lower limit is calculated, in addition to an upper limit and a predicted value. These functions are shown in equations (6)–(8) with coefficients listed in Tables 1–3 for all four local time sectors. This result allows for a coarse prediction for the electron number density, temperature, and energy density at GEO for intervals of 12 h in the future (within given confidence levels), given an instantaneous solar wind velocity. These functions and corresponding coefficients are then tested on GOES-13 data from 2012 and are shown to follow the overarching trend of the observed values.

The temperature distributions, when observed over the range of time delays applied in this study, are consistent with the heating of a low-energy population by elevated solar wind velocity. This is apparent in Figure 4 as an increasing gradient of the calculated velocity-dependent lower limit once a time delay is applied (i.e., several hours following an observation of elevated solar wind velocity, it is unlikely that the temperature of electrons at GEO will be low). This is consistent with the results of *Borovsky and Denton* [2010].

From testing the calculated prediction functions (Figure 6), it appears that the calculated electron number density, N, and energy density, $\mathcal{E}$, follow the general trend of observations more cleanly than the electron temperature, T, via the methodology used in this study. Given that electron number density and temperature are the fundamental physical parameters of a plasma, the result is a testable model that addresses elementary plasma properties. Hence, for a Maxwellian plasma, it is possible to infer the flux at any energy, not just energy channels tied to a particular instrument. The electron energy density at GEO is not a quantity that has been widely considered in recent publications. Perhaps with the direct relationship to solar wind velocity highlighted in this study, it is a quantity that could be further examined in research of radiation belt

dynamics. Additionally, it may be beneficial for future studies to consider other candidate solar wind drivers in addition to the solar wind velocity. While using solely this parameter has been shown to be capable of obtaining a coarse prediction of the partial moments from GOES-13, obviously it does not capture all of the short time scale variability.

In conclusion,

1. The electron temperature, electron number density, and electron energy density variations at GEO display a dependence on the solar wind proton density; however, the relationship with solar wind velocity is more well defined.
2. Both elevated electron temperature and elevated electron number density in the outer electron radiation belt can occur over a broad range of solar wind velocities. For both elevated electron temperature and elevated electron number density to occur simultaneously, fast solar wind is usually observed approximately 24 h previous.
3. The electron number density at GEO displays similar characteristics to the structure observed in the fluxes described by *Paulikas and Blake* [1979] and more recently by *Reeves et al.* [2011] (triangle distribution). The electron number density at GEO is subject to a solar wind velocity-dependent lower limit.
4. The electron temperature at GEO does not display a velocity-dependent lower limit when compared with the instantaneous solar wind velocity. However, with increasing time lag, a velocity-dependent lower limit does become more apparent (i.e., the temperature of the electron distribution at GEO increases during the fast solar wind following the passing of a corotating interaction region).
5. Considering the electron energy density instead of the electron temperature improves the correlation of this moment with solar wind velocity (due to the removal of the number density term in the denominator of the temperature integrals). The electron energy density is subject to a solar wind velocity-dependent lower limit.
6. It is possible, given a solar wind velocity, to obtain a coarse prediction of the electron number density, temperature, and energy density at GEO (within given confidence limits) at some time in the future. These predictions, and 90% confidence limits, are defined using equations (6)–(8) with coefficients listed in Tables 1–3 for electron number density, temperature, and energy density, respectively, for all local time sectors.

Acknowledgments

Research at Lancaster is supported by a Science and Technology Facilities Council (STFC) studentship grant. D.P. Hartley would like to thank the Royal Astronomical Society Conference Travel Fund and the Institute of Physics Research Student Conference Fund and C R Barber Trust. M.H. Denton is supported by STFC grant ST/I000801/1. OMNI data were obtained from the GSFC/SPDF OMNIWeb interface at http://omniweb.gsfc.nasa.gov. The development of the GOES moments algorithm and software at CIRES was supported by the GOES-R Risk Reduction Program.

Michael Liemohn thanks the reviewers for their assistance in evaluating this paper.

References

Baker, D. N., R. W. Klebesadel, P. R. Higbie, and J. B. Blake (1986), Highly relativistic electrons in the Earth's outer magnetosphere: 1. Lifetimes and temporal history 1979–1984, *J. Geophys. Res.*, *91*, 4265–4276.

Baker, D. N., S. G. Kanekal, T. I. Pulkkinen, and J. B. Blake (1999), Equinoctial and solstitial averages of magnetospheric relativistic electrons: A strong semiannual modulation, *Geophys. Res. Lett.*, *26*(20), 3193–3196.

Balikhin, M. A., R. J. Boynton, S. N. Walker, J. E. Borovsky, S. A. Billings, and H. L. Wei (2011), Using the NARMAX approach to model the evolution of energetic electrons fluxes at geostationary orbit, *Geophys. Res. Lett.*, *38*, L18105, doi:10.1029/2011GL048980.

Borovsky, J. E., M. F. Thomsen, D. J. McComas, T. E. Cayton, and D. J. Knipp (1998), Magnetospheric dynamics and mass flow during the November 1993 storm, *J. Geophys. Res.*, *103*, 26,373–26,394, doi:10.1029/97JA03051.

Borovsky, J. E., and M. H. Denton (2006), Differences between CME-driven storms and CIR-driven storms, *J. Geophys. Res.*, *111*, A07S08, doi:10.1029/2005JA011447.

Borovsky, J. E., and M. H. Denton (2009), Relativistic-electron dropouts and recovery: A superposed epoch study of the magnetosphere and the solar wind, *J. Geophys. Res.*, *114*, A02201, doi:10.1029/2008JA013128.

Borovsky, J. E., and M. H. Denton (2010), On the heating of the outer radiation belt to produce high fluxes of relativistic electrons: Measured heating rates at geosynchronous orbit for high-speed stream-driven storms, *J. Geophys. Res.*, *115*, A12206, doi:10.1029/2010JA015342.

Borovsky, J. E., and T. E. Cayton (2011), Entropy mapping of the outer electron radiation belt between the magnetotail and geosynchronous orbit, *J. Geophys. Res.*, *116*, A06216, doi:10.1029/2011JA016470.

Boynton, R. J., M. A. Balikhin, S. A. Billings, G. D. Reeves, N. Ganushkina, M. Gedalin, O. A. Amariutei, J. E. Borovsky, and S. N. Walker (2013), The analysis of electron fluxes at geosynchronous orbit employing a NARMAX approach, *J. Geophys. Res. Space Physics*, *118*, 1500–1513, doi:10.1002/jgra.50192.

Cayton, T. E., R. D. Belian, S. P. Gary, T. A. Fritz, and D. N. Baker (1989), Energetic electron components at geosynchronous orbit, *Geophys. Res. Lett.*, *16*, 147–150, doi:10.1029/GL016i002p00147.

Chen, Y., G. D. Reeves, and R. H. Friedel (2007), The energization of relativistic electrons in the outer Van Allen radiation belt, *Nat. Phys.*, *3*, 614–617, doi:10.1038/nphys655.

Christon, S. P., D. G. Mitchell, D. J. Williams, L. A. Frank, C. Y. Huang, and T. E. Eastman (1988), Energy spectra of plasma sheet ions and electrons from 50 eV/e to 1 MeV during plasma temperature transitions, *J. Geophys. Res.*, *93*(A4), 2562–2572, doi:10.1029/JA093iA04p02562.

Clilverd, M. A., N. Cobbett, C. J. Rodger, J. B. Brundell, M. H. Denton, D. P. Hartley, J. V. Rodriguez, D. Danskin, T. Raita, and E. L. Spanswick (2013), Energetic electron precipitation characteristics observed from Antarctica during a flux dropout event, *J. Geophys. Res. Space Physics*, *118*, 6921–6935, doi:10.1002/2013JA019067.

Daglis, I. A., S. Livi, E. T. Sarris, and B. Wilken (1994), Energy density of ionospheric and solar wind origin ions in the near-Earth magnetotail during substorms, *J. Geophys. Res.*, *99*(A4), 5691–5703, doi:10.1029/93JA02772.

Denton, M. H., and J. E. Borovsky (2009), The superdense plasma sheet in the magnetosphere during high-speed-steam-driven storms: Plasma transport time scales, *J. Atmos. Sol. Terr. Phys.*, *71*, 1045–1058.
Denton, M. H., J. E. Borovsky, and T. E. Cayton (2010), A density-temperature description of the outer electron radiation belt during geomagnetic storms, *J. Geophys. Res.*, *115*, A01208, doi:10.1029/2009JA014183.
Denton, M. H., and T. E. Cayton (2011), Density and temperature of energetic electrons in the Earth's magnetotail derived from high-latitude GPS observations during the declining phase of the solar cycle, *Ann. Geophys.*, *29*, 1755–1763, doi:10.5194/angeo-29-1755-2011.
Freeman, J. W. (1964), The morphology of the electron distribution in the outer radiation zone and near the magnetospheric boundary as observed by Explorer 12, *J. Geophys. Res.*, *69*, 1691–1723.
Friedel, R. H. W., G. D. Reeves, and T. Obara (2002), Relativistic electron dynamics in the inner magnetosphere: A review, *J. Atmos. Sol. Terr. Phys.*, *64*, 265–282, doi:10.1016/S1364-6826(01)00088-8.
Fukata, M., S. Taguchi, T. Okuzawa, and T. Obara (2002), Neural network prediction of relativistic electrons at geosynchronous orbit during the storm recovery phase: Effects of recurring substorms, *Ann. Geophys.*, *20*, 947–951, doi:10.5194/angeo-20-947-2002.
Gary, S. P. (1993), *Theory of Space Plasma Microinstabilities*, Cambridge Univ. Press, New York.
Gkioulidou, M., C.-P. Wang, L. R. Lyons, and R. A. Wolf (2009), Formation of the Harang reversal and its dependence on plasma sheet conditions: Rice convection model simulations, *J. Geophys. Res.*, *114*, A07204, doi:10.1029/2008JA013955.
Green, J. C., T. G. Onsager, T. P. O'Brien, and D. N. Baker (2004), Testing loss mechanisms capable of rapidly depleting relativistic electron flux in the Earth's outer radiation belt, *J. Geophys. Res.*, *109*, A12211, doi:10.1029/2004JA010579.
Gurgiolo, C., C. Lin, B. Mauk, G. K. Parks, and C. McIlwain (1979), Plasma injection and diamagnetism, *J. Geophys. Res.*, *84*(A5), 2049–2056, doi:10.1029/JA084iA05p02049.
Hartley, D. P., M. H. Denton, J. C. Green, T. G. Onsager, J. V. Rodriguez, and H. J. Singer (2013), Case studies of the impact of high-speed solar wind streams on the electron radiation belt at geosynchronous orbit: Flux, magnetic field, and phase space density, *J. Geophys. Res. Space Physics*, *118*, 6964–6979, doi:10.1002/2013JA018923.
Horne, R. B., S. A. Glauert, N. P. Meredith, D. Boscher, V. Maget, D. Heynderickx, and D. Pitchford (2013), Space weather impacts on satellites and forecasting the Earth's electron radiation belts with SPACECAST, *Space Weather*, *11*, 169–186, doi:10.1002/swe.20023.
Hudson, M. K., S. R. Elkington, J. G. Lyon, V. A. Marchenko, I. Roth, M. Temerin, J. B. Blake, M. S. Gussenhoven, and J. R. Wygant (1997), Simulations of radiation belt formation during storm sudden commencements, *J. Geophys. Res.*, *102*(A7), 14,087–14,102, doi:10.1029/97JA03995.
Hudson, M. K., B. T. Kress, H.-R. Mueller, J. A. Zastrow, and J. B. Blake (2008), Relationship of the Van Allen radiation belts to solar wind drivers, *J. Atmos. Sol. Terr. Phys.*, *70*, 708–729, doi:10.1016/j.jastp.2007.11.003.
Johansson, R. (1993), *System Modeling and Identification*, Prentice-Hall, Old Tappan, N. J.
King, J. H., and N. E. Papitashvili (2005), Solar wind spatial scales in and comparisons of hourly Wind and ACE plasma and magnetic field data, *J. Geophys. Res.*, *110*, A02104, doi:10.1029/2004JA010649.
Koons, H. C., and D. J. Gorney (1991), A neural network model of the relativistic electron flux at geosynchronous orbit, *J. Geophys. Res.*, *96*, 5549.
Li, X., D. N. Baker, M. Temerin, G. Reeves, R. Friedel, and C. Shen (2005), Energetic electrons, 50 keV to 6 MeV, at geosynchronous orbit: Their responses to solar wind variations, *Space Weather*, *3*, S04001, doi:10.1029/2004SW000105.
Liemohn, M. W., and A. A. Chan (2007), Unravelling the causes of radiation belt enhancements, *Eos Trans. AGU*, *88*(42), 425–426, doi:10.1029/2007EO420001.
Ljung, L. (1999), *System Identification: Theory for the User,* 2nd ed., Prentice Hall PTF, Upper Saddle River, N. J.
MacDonald, E. A., M. H. Denton, M. F. Thomsen, and S. P. Gary (2008), Superposed epoch analysis of a whistler instability criterion at geosynchronous orbit during geomagnetic storms, *J. Atmos. Sol. Terr. Phys.*, *70*, 1789–1796, doi:/10.1016/j.jastp.2008.03.021.
Mann, I. R., T. P. O'Brien, and D. K. Milling (2004), Correlations between ULF wave power, solar wind speed, and relativistic electron flux in the magnetosphere: Solar cycle dependence, *J. Atmos. Sol. Terr. Phys.*, *66*, 187–198, doi:10.1016/j.jastp.2003.10.002.
McPherron, R. L., D. N. Baker, and N. U. Crooker (2009), Role of the Russell McPherron effect in the acceleration of relativistic electrons, *J. Atmos. Sol. Terr. Phys.*, *71*(10–11), 1032–1044, doi:10.1016/j.jastp.2008.11.002.
Millan, R. M., and R. M. Thorne (2007), Review of radiation belt relativistic electron losses, *J. Atmos. Sol. Terr. Phys.*, *69*, 362–377, doi:10.1016/j.jastp.2006.06.019.
Miyoshi, Y., and R. Kataoka (2008), Flux enhancement of the outer radiation belt electrons after the arrival of stream interaction regions, *J. Geophys. Res.*, *113*, A03S09, doi:10.1029/2007JA012506.
Morley, S. K., R. H. W. Friedel, E. L. Spanswick, G. D. Reeves, J. T. Steinberg, J. Koller, T. Cayton, and E. Noveroske (2010), Dropouts of the outer electron radiation belt in response to solar wind stream interfaces: Global positioning system observations, *Proc. R. Soc. London, Ser. A*, *2010*, 466, doi:10.1098/rspa.2010.0078.
Nagai, T. (1988), Space weather forecast prediction of relativistic electron intensity at synchronous orbit, *Geophys. Res. Lett.*, *15*, 425–428.
Nelles, O. (2001), *Nonlinear System Identification*, Springer-Verlag, New York.
O'Brien, T. P., R. L. McPherron, D. Sornette, G. D. Reeves, R. Friedel, and H. J. Singer (2001), Which magnetic storms produce relativistic electrons at geosynchronous orbit, *J. Geophys. Res.*, *106*, 15,533–15,544.
Onsager, T. G., et al. (2002), Radiation belt electron flux dropouts: Local time, radial, and particle-energy dependence, *J. Geophys. Res.*, *107*(A11), 1382, doi:10.1029/2001JA000187.
Onsager, T. G., A. A. Chan, Y. Fei, S. R. Elkington, J. C. Green, and H. J. Singer (2004), The radial gradient of relativistic electrons at geosynchronous orbit, *J. Geophys. Res.*, *109*, A05221, doi:10.1029/2003JA010368.
Onsager, T. G., J. C. Green, G. D. Reeves, and H. J. Singer (2007), Solar wind and magnetospheric conditions leading to the abrupt loss of outer radiation belt electrons, *J. Geophys. Res.*, *112*, A01202, doi:10.1029/2006JA011708.
Paulikas, G. A., and J. B. Blake (1979), Effects of the solar wind on magnetospheric dynamics: Energetic electrons at the synchronous orbit, in *Quantitative Modeling of Magnetospheric Processes, Geophys. Monogr. Ser.*, vol. 21, edited by W. P. Oslon, pp. 180–202, AGU, Washington, D. C.
Reeves, G. D., K. L. McAdams, R. H. W. Friedel, and T. P. O'Brien (2003), Acceleration and loss of relativistic electrons during geomagnetic storms, *Geophys. Res. Lett.*, *30*, 1529, doi:10.1029/2002GL016513.
Reeves, G. D., S. K. Morley, R. H. W. Friedel, M. G. Henderson, T. E. Cayton, G. Cunningham, J. B. Blake, R. A. Christensen, and D. Thomsen (2011), On the relationship between relativistic electron flux and solar wind velocity: Paulikas and Blake revisited, *J. Geophys. Res.*, *116*, A02213, doi:10.1029/2010JA015735.

Reeves, G. D., S. K. Morley, and G. Cunningham (2013), Long-term variations in solar wind velocity and radiation belt electrons, *J. Geophys. Res. Space Physics*, *118*, 1040–1048, doi:10.1002/jgra.50126.

Scudder, J. D. (1992), On the causes of temperature change in inhomogeneous low-density astrophysical plasmas, *Astrophys. J.*, *398*, 299.

Weigel, R. S., A. J. Klimas, and D. Vassiliadis (2003), Precursor analysis and prediction of large-amplitude relativistic electron fluxes, *Space Weather*, *1*(3), 1014, doi:10.1029/2003SW000023.